The Astrophysical Journal, 835:151 (15pp), 2017 February 1 doi:10.3847/1538-4357/835/2/151

All-sky Search for Time-integrated Neutrino Emission from Astrophysical Sources with 7 yr of IceCube Data

M. G. Aartsen[1], K. Abraham[2], M. Ackermann[3], J. Adams[4], J. A. Aguilar[5], M. Ahlers[6], M. Ahrens[7], D. Altmann[8], K. Andeen[9], T. Anderson[10], I. Ansseau[5], G. Anton[8], M. Archinger[11], C. Argüelles[12], J. Auffenberg[13], S. Axani[12], X. Bai[14], S. W. Barwick[15], V. Baum[11], R. Bay[16], J. J. Beatty[17,18], J. Becker Tjus[19], K.-H. Becker[20], S. BenZvi[21], D. Berley[22], E. Bernardini[3], A. Bernhard[2], D. Z. Besson[23], G. Binder[16,24], D. Bindig[20], M. Bissok[13], E. Blaufuss[22], S. Blot[3], C. Bohm[7], M. Börner[25], F. Bos[19], D. Bose[26], S. Böser[11], O. Botner[27], J. Braun[6], L. Brayeur[28], H.-P. Bretz[3], S. Bron[29], A. Burgman[27], T. Carver[29], M. Casier[28], E. Cheung[22], D. Chirkin[6], A. Christov[29], K. Clark[30], L. Classen[31], S. Coenders[2], G. H. Collin[12], J. M. Conrad[12], D. F. Cowen[10,32], R. Cross[21], M. Day[6], J. P. A. M. de André[33], C. De Clercq[28], E. del Pino Rosendo[11], H. Dembinski[34], S. De Ridder[35], P. Desiati[6], K. D. de Vries[28], G. de Wasseige[28], M. de With[36], T. DeYoung[33], J. C. Díaz-Vélez[6], V. di Lorenzo[11], H. Dujmovic[26], J. P. Dumm[7], M. Dunkman[10], B. Eberhardt[11], T. Ehrhardt[11], B. Eichmann[19], P. Eller[10], S. Euler[27], P. A. Evenson[34], S. Fahey[6], A. R. Fazely[37], J. Feintzeig[6], J. Felde[22], K. Filimonov[16], C. Finley[7], S. Flis[7], C.-C. Fösig[11], A. Franckowiak[3], E. Friedman[22], T. Fuchs[25], T. K. Gaisser[34], J. Gallagher[38], L. Gerhardt[16,24], K. Ghorbani[6], W. Giang[39], L. Gladstone[6], T. Glauch[13], T. Glüsenkamp[3], A. Goldschmidt[24], G. Golup[28], J. G. Gonzalez[34], D. Grant[39], Z. Griffith[6], C. Haack[13], A. Haj Ismail[35], A. Hallgren[27], F. Halzen[6], E. Hansen[40], T. Hansmann[13], K. Hanson[6], D. Hebecker[36], D. Heereman[5], K. Helbing[20], R. Hellauer[22], S. Hickford[20], J. Hignight[33], G. C. Hill[1], K. D. Hoffman[22], R. Hoffmann[20], K. Holzapfel[2], K. Hoshina[6,41], F. Huang[10], M. Huber[2], K. Hultqvist[7], S. In[26], A. Ishihara[42], E. Jacobi[3], G. S. Japaridze[43], M. Jeong[26], K. Jero[6], B. J. P. Jones[12], M. Jurkovic[2], A. Kappes[31], T. Karg[3], A. Karle[6], U. Katz[8], M. Kauer[6], A. Keivani[10], J. L. Kelley[6], A. Kheirandish[6], M. Kim[26], T. Kintscher[3], J. Kiryluk[44], T. Kittler[8], S. R. Klein[16,24], G. Kohnen[45], R. Koirala[34], H. Kolanoski[36], R. Konietz[13], L. Köpke[11], C. Kopper[39], S. Kopper[20], D. J. Koskinen[40], M. Kowalski[3,36], K. Krings[2], M. Kroll[19], G. Krückl[11], C. Krüger[6], J. Kunnen[28], S. Kunwar[3], N. Kurahashi[46], T. Kuwabara[42], M. Labare[35], J. L. Lanfranchi[10], M. J. Larson[40], F. Lauber[20], D. Lennarz[33], M. Lesiak-Bzdak[43], M. Leuermann[13], L. Lu[42], J. Lünemann[28], J. Madsen[47], G. Maggi[28], K. B. M. Mahn[33], S. Mancina[6], M. Mandelartz[19], R. Maruyama[48], K. Mase[42], R. Maunu[22], F. McNally[6], K. Meagher[5], M. Medici[40], M. Meier[25], A. Meli[35], T. Menne[25], G. Merino[6], T. Meures[5], S. Miarecki[16,24], L. Mohrmann[3], T. Montaruli[29], M. Moulai[12], R. Nahnhauer[3], U. Naumann[20], G. Neer[33], H. Niederhausen[43], S. C. Nowicki[39], D. R. Nygren[24], A. Obertacke Pollmann[20], A. Olivas[22], A. O'Murchadha[5], T. Palczewski[49], H. Pandya[34], D. V. Pankova[10], P. Peiffer[11], Ö. Penek[13], J. A. Pepper[49], C. Pérez de los Heros[27], D. Pieloth[25], E. Pinat[5], P. B. Price[16], G. T. Przybylski[24], M. Quinnan[10], C. Raab[5], L. Rädel[13], M. Rameez[40], K. Rawlins[50], R. Reimann[13], B. Relethford[46], M. Relich[42], E. Resconi[2], W. Rhode[25], M. Richman[46], B. Riedel[39], S. Robertson[1], M. Rongen[13], C. Rott[26], T. Ruhe[25], D. Ryckbosch[35], D. Rysewyk[33], L. Sabbatini[6], S. E. Sanchez Herrera[39], A. Sandrock[25], J. Sandroos[11], S. Sarkar[40,51], K. Satalecka[3], P. Schlunder[25], T. Schmidt[22], S. Schoenen[13], S. Schöneberg[19], L. Schumacher[13], D. Seckel[34], S. Seunarine[47], D. Soldin[20], M. Song[22], G. M. Spiczak[47], C. Spiering[3], T. Stanev[34], A. Stasik[3], J. Stettner[13], A. Steuer[11], T. Stezelberger[24], R. G. Stokstad[24], A. Stössl[3], R. Ström[27], N. L. Strotjohann[3], G. W. Sullivan[22], M. Sutherland[17], H. Taavola[27], I. Taboada[52], J. Tatar[16,24], F. Tenholt[19], S. Ter-Antonyan[37], A. Terliuk[3], G. Tešić[10], S. Tilav[34], P. A. Toale[49], M. N. Tobin[6], S. Toscano[28], D. Tosi[6], M. Tselengidou[8], A. Turcati[2], E. Unger[27], M. Usner[3], J. Vandenbroucke[6], N. van Eijndhoven[28], S. Vanheule[35], M. van Rossem[6], J. van Santen[3], J. Veenkamp[2], M. Vehring[13], M. Voge[53], E. Vogel[13], M. Vraeghe[35], C. Walck[7], A. Wallace[1], M. Wallraff[13], N. Wandkowsky[6], Ch. Weaver[39], M. J. Weiss[10], C. Wendt[6], S. Westerhoff[6], B. J. Whelan[1], S. Wickmann[13], K. Wiebe[11], C. H. Wiebusch[13], L. Wille[6], D. R. Williams[48], L. Wills[45], M. Wolf[7], T. R. Wood[39], E. Woolsey[39], K. Woschnagg[16], D. L. Xu[6], X. W. Xu[37], Y. Xu[43], J. P. Yanez[3], G. Yodh[15], S. Yoshida[42], and M. Zoll[7]
(IceCube Collaboration)

[1] Department of Physics, University of Adelaide, Adelaide, 5005, Australia
[2] Physik-department, Technische Universität München, D-85748 Garching, Germany
[3] DESY, D-15735 Zeuthen, Germany
[4] Dept. of Physics and Astronomy, University of Canterbury, Private Bag 4800, Christchurch, New Zealand
[5] Université Libre de Bruxelles, Science Faculty CP230, B-1050 Brussels, Belgium
[6] Dept. of Physics and Wisconsin IceCube Particle Astrophysics Center, University of Wisconsin, Madison, WI 53706, USA
[7] Oskar Klein Centre and Dept. of Physics, Stockholm University, SE-10691 Stockholm, Sweden
[8] Erlangen Centre for Astroparticle Physics, Friedrich-Alexander-Universität Erlangen-Nürnberg, D-91058 Erlangen, Germany
[9] Department of Physics, Marquette University, Milwaukee, WI 53201, USA
[10] Dept. of Physics, Pennsylvania State University, University Park, PA 16802, USA
[11] Institute of Physics, University of Mainz, Staudinger Weg 7, D-55099 Mainz, Germany
[12] Dept. of Physics, Massachusetts Institute of Technology, Cambridge, MA 02139, USA
[13] III. Physikalisches Institut, RWTH Aachen University, D-52056 Aachen, Germany
[14] Physics Department, South Dakota School of Mines and Technology, Rapid City, SD 57701, USA
[15] Dept. of Physics and Astronomy, University of California, Irvine, CA 92697, USA
[16] Dept. of Physics, University of California, Berkeley, CA 94720, USA
[17] Dept. of Physics and Center for Cosmology and Astro-Particle Physics, Ohio State University, Columbus, OH 43210, USA
[18] Dept. of Astronomy, Ohio State University, Columbus, OH 43210, USA
[19] Fakultät für Physik & Astronomie, Ruhr-Universität Bochum, D-44780 Bochum, Germany

[20] Dept. of Physics, University of Wuppertal, D-42119 Wuppertal, Germany
[21] Dept. of Physics and Astronomy, University of Rochester, Rochester, NY 14627, USA
[22] Dept. of Physics, University of Maryland, College Park, MD 20742, USA
[23] Dept. of Physics and Astronomy, University of Kansas, Lawrence, KS 66045, USA
[24] Lawrence Berkeley National Laboratory, Berkeley, CA 94720, USA
[25] Dept. of Physics, TU Dortmund University, D-44221 Dortmund, Germany
[26] Dept. of Physics, Sungkyunkwan University, Suwon 440-746, Korea
[27] Dept. of Physics and Astronomy, Uppsala University, Box 516, SE-75120 Uppsala, Sweden
[28] Vrije Universiteit Brussel, Dienst ELEM, B-1050 Brussels, Belgium
[29] Département de physique nucléaire et corpusculaire, Université de Genève, CH-1211 Genève, Switzerland
[30] Dept. of Physics, University of Toronto, Toronto, ON M5S 1A7, Canada
[31] Institut für Kernphysik, Westfälische Wilhelms-Universität Münster, D-48149 Münster, Germany
[32] Dept. of Astronomy and Astrophysics, Pennsylvania State University, University Park, PA 16802, USA
[33] Dept. of Physics and Astronomy, Michigan State University, East Lansing, MI 48824, USA
[34] Bartol Research Institute and Dept. of Physics and Astronomy, University of Delaware, Newark, DE 19716, USA
[35] Dept. of Physics and Astronomy, University of Gent, B-9000 Gent, Belgium
[36] Institut für Physik, Humboldt-Universität zu Berlin, D-12489 Berlin, Germany
[37] Dept. of Physics, Southern University, Baton Rouge, LA 70813, USA
[38] Dept. of Astronomy, University of Wisconsin, Madison, WI 53706, USA
[39] Dept. of Physics, University of Alberta, Edmonton, AB T6G 2E1, Canada
[40] Niels Bohr Institute, University of Copenhagen, DK-2100 Copenhagen, Denmark
[41] Earthquake Research Institute, University of Tokyo, Bunkyo, Tokyo 113-0032, Japan
[42] Dept. of Physics and Institute for Global Prominent Research, Chiba University, Chiba 263-8522, Japan
[43] CTSPS, Clark-Atlanta University, Atlanta, GA 30314, USA
[44] Dept. of Physics and Astronomy, Stony Brook University, Stony Brook, NY 11794-3800, USA
[45] Université de Mons, B-7000 Mons, Belgium
[46] Dept. of Physics, Drexel University, 3141 Chestnut Street, Philadelphia, PA 19104, USA
[47] Dept. of Physics, University of Wisconsin, River Falls, WI 54022, USA
[48] Dept. of Physics, Yale University, New Haven, CT 06520, USA
[49] Dept. of Physics and Astronomy, University of Alabama, Tuscaloosa, AL 35487, USA
[50] Dept. of Physics and Astronomy, University of Alaska Anchorage, 3211 Providence Drive, Anchorage, AK 99508, USA
[51] Dept. of Physics, University of Oxford, 1 Keble Road, Oxford OX1 3NP, UK
[52] School of Physics and Center for Relativistic Astrophysics, Georgia Institute of Technology, Atlanta, GA 30332, USA
[53] Physikalisches Institut, Universität Bonn, Nussallee 12, D-53115 Bonn, Germany
Received 2016 September 16; revised 2016 December 6; accepted 2016 December 6; published 2017 January 24

Abstract

Since the recent detection of an astrophysical flux of high-energy neutrinos, the question of its origin has not yet fully been answered. Much of what is known about this flux comes from a small event sample of high neutrino purity, good energy resolution, but large angular uncertainties. In searches for point-like sources, on the other hand, the best performance is given by using large statistics and good angular reconstructions. Track-like muon events produced in neutrino interactions satisfy these requirements. We present here the results of searches for point-like sources with neutrinos using data acquired by the IceCube detector over 7 yr from 2008 to 2015. The discovery potential of the analysis in the northern sky is now significantly below $E_\nu^2 d\phi/dE_\nu = 10^{-12}\,\mathrm{TeV\,cm^{-2}\,s^{-1}}$, on average 38% lower than the sensitivity of the previously published analysis of 4 yr exposure. No significant clustering of neutrinos above background expectation was observed, and implications for prominent neutrino source candidates are discussed.

Key words: astroparticle physics – galaxies: active – neutrinos

1. Introduction

One outstanding question in astroparticle physics is the origin of ultra-high-energy cosmic rays (UHECRs). In the paradigm of multi-messenger astronomy, both photons and neutrinos can help resolve the sources of UHECRs (Beatty & Westerhoff 2009; Kotera & Olinto 2011). Photons and neutrinos are believed to be produced in the astrophysical beam dump of cosmic-ray particles interacting with matter at the source location. Due to a lack of electric charge, they point back to their origin, whereas cosmic rays are deflected by tangled magnetic fields in the universe. Sources of high-energy γ-rays in our Galaxy and extragalactic objects are detected over a wide range of energies (Hinton & Hofmann 2009), but both hadronic and leptonic processes can produce γ-rays. Neutrinos, on the other hand, trace hadronic interactions and therefore are a smoking-gun signature of cosmic-ray acceleration (Learned & Mannheim 2000; Halzen & Hooper 2002; Anchordoqui & Montaruli 2010; Anchordoqui et al. 2014). Other possible types of sources could be hidden in γ-rays and only identified using neutrinos (Murase et al. 2016; Senno et al. 2016).

IceCube recently reported the first observation of high-energy astrophysical neutrinos with more than 5σ significance (Aartsen et al. 2013a, 2014c). Neutrinos with energies up to and exceeding 1 PeV are observed in events starting inside the detector. Since then, this result is confirmed in other detection channels of interactions of $\nu_\mu + \bar{\nu}_\mu$ in the northern sky (Aartsen et al. 2015c, 2016b). The overall flux observed is consistent so far with an isotropic emission over the full sky and all neutrino flavors (Aartsen et al. 2015a, 2015d).

This paper presents the most recent results of searches for point-like steady emission of neutrinos using track-like events traversing the IceCube detector. The statistics are increased by adding 3 yr of exposure to the previous analyses (Abbasi et al. 2011; Aartsen et al. 2013c, 2014e). A sample of 712,830 events is obtained during 7 yr of data recording through 2015

June. In addition, starting tracks are used in a separate sample to help access lower energies in the southern sky (Aartsen et al. 2016a).

In Section 2, the IceCube Neutrino Observatory is introduced and the two samples of through-going and starting tracks are characterized. In Section 3, the statistical method of unbinned likelihood maximization for clustering searches is discussed. Section 4 presents the results and their implications regarding neutrino sources, and in Section 5 conclusions are drawn.

2. The Icecube Neutrino Observatory

Interactions of neutrinos in IceCube are detected using Cerenkov light emitted by relativistic charged secondary particles. To serve this purpose, one cubic kilometer of Antarctic ice was instrumented at the South Pole (Achterberg et al. 2006). A total of 5160 digital optical modules (DOMs) detect light emission in the ice at a depth ranging from 145 to 2450 m. The DOMs consist of a photomultiplier tube, electronics for digitization, and LEDs for detector calibration (Abbasi et al. 2009, 2010). DOMs are attached to 86 cables (called *strings*) in groups of 60 with vertical spacing of 17 m; the mean distance between neighboring strings is ∼125 m. The eight innermost strings form a denser sub-array called *DeepCore*, which targets lower energies (Abbasi et al. 2012). The South Pole IceCube Neutrino Observatory includes the surface array called *IceTop* (Abbasi et al. 2013) that detects and reconstructs air showers above 300 TeV using 82 ice tanks. In the analysis presented here, IceTop's capabilities are used to veto cosmic-ray-induced backgrounds.

2.1. Neutrino Detection Channels

Three event topologies are taken into account when considering neutrino interactions in IceCube. *Tracks* are induced by muons traversing the detector. Below 700 GeV, muons lose energy mainly due to ionization; above 700 GeV, stochastic energy losses due to radiative emission become the dominant component. At TeV energies, muons travel long distances, larger than several kilometers in the Antarctic ice (Chirkin & Rhode 2004). Light is constantly emitted along the track. The resulting long lever arm gives a good reconstruction performance with median angular resolution $\Delta\Psi < 1°$.[54] Moreover, the event rate greatly increases because neutrinos can interact far outside the detector prior to the detection of the secondary muon with IceCube. Charged-current interactions of electron or tau neutrinos, as well as neutral current interactions of any neutrino type, produce *shower*- or *cascade*-like events. These types of interactions produce almost spherically symmetric light emission, giving a median angular resolution of ∼10°. Another topology is induced by very high energy charged-current $\nu_\tau + \bar{\nu}_\tau$ interactions with the tau lepton decaying to hadrons after traveling a distance of $\sim 50\,\mathrm{m\,PeV}^{-1} \times E_\tau$, resulting in two cascades separated distinctly. Such a *double-bang* has not been observed so far (Aartsen et al. 2016c).

Track-like events are more suited than cascades to search for very localized (point-like), faint sources using high statistics and good angular resolution. Such events originate primarily in neutrino charged-current interactions of muon (anti)neutrinos with nucleons, but also in similar interactions of tau neutrinos with the tau lepton decaying to muons and neutrinos, or interactions of electron antineutrinos with electrons by resonant s-channel W^- exchange (*Glashow resonance*; Glashow 1960). The energy of a muon track is restricted to the fraction of the track visible in the detector, limiting the energy estimation to the *deposited energy* in the detector or the muon energy upon entering the detector. Independent of the details of neutrino production, the incident flux of astrophysical neutrinos at Earth will consist of an approximately equally shared flavor ratio for all neutrinos due to very long baseline neutrino oscillations (Athar et al. 2006). In the following, only the component of tracks created in muon neutrino interactions is taken into account as the signal of astrophysical neutrinos, likewise to Aartsen et al. (2014e) and Adrian-Martinez et al. (2014). The impact of track events originating from other neutrino interactions is discussed in Section 3.5.

Construction of IceCube finished in 2010 December after 6 yr of deployment. During construction, partial configurations of the detector were successfully taking data, commonly indicated by IC*XY*, with *XY* denoting the number of active strings. The first 3 yr of the event sample are in partial detector configurations IC40, IC59, and IC79. The previously published analysis (Aartsen et al. 2014e) included the first year of data-taking with the completed detector IC86 and 3 yr in partial configuration (Abbasi et al. 2011; Aartsen et al. 2013c). These samples focus on through-going track-like events, yielding high statistics over broad energy ranges. In the southern sky, an additional selection of starting tracks, which has a greatly reduced background rate, is performed in order to access lower energies (Aartsen et al. 2016a). This uses completely independent events to the ones selected in the aforementioned through-going track channel.

The details of all samples are listed in Table 1, including the exposure time and sample size. In this work, the detector livetime is increased by adding data from 2012 June to 2015 June to the analysis, thus increasing the livetime by 1058 days, to a total of 2431 days. The sample of starting tracks (Aartsen et al. 2016a) has an increased livetime of 2 yr to a total of 1715 days that coincide with the five most recent years of the through-going track event sample, starting with IC79.

Table 1
IceCube Samples Used in This Analysis

Sample	Livetime (days)	atm. ν (day^{-1})	Up-going Events	Down-going Events
IC40	376	40	16323	20577
IC59	348	120	48105	58906
IC79	316	180	54823	38310
IC86	333	210	67938	68302
2012–2015	1058	220	235602	102983
Σ	2431	⋯	422791	289078
Starting tracks	1715	<0.03	0	961

Note. For each sample, characteristic features are quoted, separated in the two halves of the sky. Previously published results used 4 yr of data: IC40 (Abbasi et al. 2011), IC59+IC79 (Aartsen et al. 2013c), and the first year of IC86 (Aartsen et al. 2014e). Data taken in the seasons from 2012 to 2015 are added in this paper. The separation in the two regions is done at a declination of $\delta = -5°$. In addition, starting tracks are used in a separate sample (Aartsen et al. 2016a), with two additional years of available data.

[54] Evaluated using dedicated Monte Carlo simulation, verified using experimental data of cosmic-ray shadowing of the Moon (Aartsen et al. 2014d).

In the following, the modeling of signal and background for both the through-going and starting track samples is described. The event selection is briefly discussed and the performance of the event sample highlighted. For more detailed information, refer to Abbasi et al. (2011), Aartsen et al. (2013c), and Aartsen et al. (2014e) for through-going muons and Aartsen et al. (2016a) for starting tracks.

In this work, muon tracks induced by astrophysical neutrino interactions are the main signal category in the search for point-like sources of neutrinos. Detailed Monte Carlo simulation is used to evaluate the response of IceCube to such events and distinguish them from atmospheric backgrounds. The median angular resolution $\Delta\Psi$ and the event rate expectation

$$\dot{N}_\nu = \int d\Omega \int_0^\infty dE\, A_{\rm eff}(E, \Omega) \times F_\nu(E_\nu, \Omega) \qquad (1)$$

given by the detector *effective area* $A_{\rm eff}$ and the incident neutrino flux F_ν can be derived from the simulation (for more information about the details of the Monte Carlo simulation used here, see Aartsen et al. 2016b).

2.2. Through-going Tracks

The main background regarding neutrino searches in IceCube consists of atmospheric muons that are created in extensive air showers and reach IceCube at a depth of ∼2 km. Almost all events triggering the detector at a rate of ∼2.8 kHz belong to this component. Similar to Aartsen et al. (2014e), the selection is split into two regions divided at the horizon (declination $\delta = -5°$) due to different background characteristics, as explained in the following.

In the northern sky (up-going region, $\delta \geqslant -5°$), the main background consists of atmospheric muon events that are misreconstructed as up-going; truly up-going muons can only originate from prior neutrino interactions, since all other muons are shielded by Earth. Hence, the atmospheric muon background is rejected by identifying poorly reconstructed events. In order to achieve this, multivariate selection techniques (boosted decision tree, BDT) are used to discriminate well-reconstructed tracks from neutrino interactions against misreconstructed background. The variables used in the BDT are connected to the event quality and a clear track-like topology. Similar to Aartsen et al. (2014e), BDTs are trained for two signal energy spectra of E^{-2} and $E^{-2.7}$, and the cut on the linear combination of BDT scores is optimized to yield the best sensitivity and discovery potential over a wide range of energies with the final cut on BDT output. These spectra are chosen to be sensitive to both hard energy spectra and soft or cutoff spectra. A neutrino-dominated sample is obtained in the northern sky. The remaining background consists of atmospheric neutrinos produced in the northern sky. These neutrinos are an irreducible background, but follow a softer energy spectrum ($\sim E^{-3.7}$–$E^{-4.0}$ or $\sim E^{-2.7}$–$E^{-3.0}$ for conventional or prompt neutrinos, respectively) than the expected signal ($\sim E^{-2}$ consistent with diffuse muon neutrino signal at 250 TeV and above; see Aartsen et al. 2016b). Figure 1 shows the effective area calculated using muon neutrino Monte Carlo simulation of the final event sample for different declination regions. In the northern sky (red, blue), a low energy threshold is achieved, while for near-vertically up-going events absorption becomes an important effect above 100 TeV. Figure 2 shows the median angular resolution of the track reconstruction (solid) with respect to the primary neutrino direction against neutrino energy. Above TeV energies, the kinematic angle (dotted) of muon and parent neutrino becomes negligible and the angular resolution is below 1°. The energy resolution of the track's energy proxy is ∼30% in $\log_{10} E$ (Aartsen et al. 2014a). This is only a lower limit on the energy of a muon that enters the detector from outside and loses energy prior to detection, as well as on energy of the primary neutrino that produced the muon in an interaction with a nucleus. For more information about the neutrino and muon energy estimation, refer to Aartsen et al. (2015c, 2016b).

In the southern sky (down-going, $\delta < -5°$), the picture changes because of large backgrounds of well-reconstructed down-going atmospheric muons. Moreover, muons are produced at high multiplicity in cosmic-ray showers, resulting in bundles of muons; such bundles produce large amounts of light in the detector, thus imitating the signature of a single muon of much higher energy. Similar to the northern sky, BDTs are used to select only the best-reconstructed events at the highest energies. Following the development of Aartsen et al. (2014e), in addition to event quality and track topology parameters, four

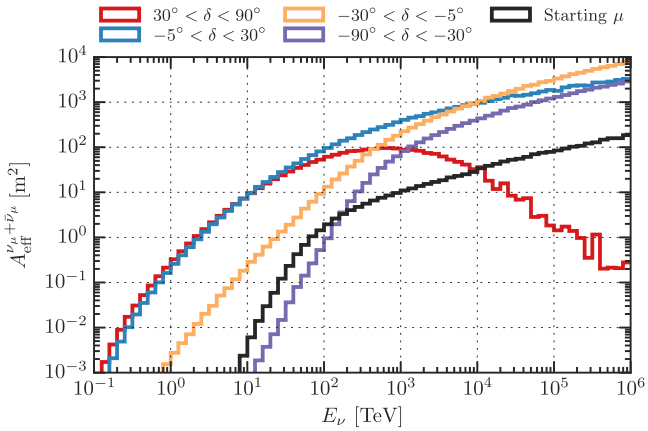

Figure 1. IceCube effective area as defined in Equation (1) vs. neutrino energy for a flux of $\nu_\mu + \bar{\nu}_\mu$ calculated using simulation of neutrino events for the selection of IC86 (seasons 2012–2015) described in Section 2.2. The effective area for through-going muons is averaged over the solid angle in the declination range (δ) indicated in the legend. Additionally, the effective area for starting tracks in the southern sky ($\delta < -5°$) is shown in black (see Section 2.3).

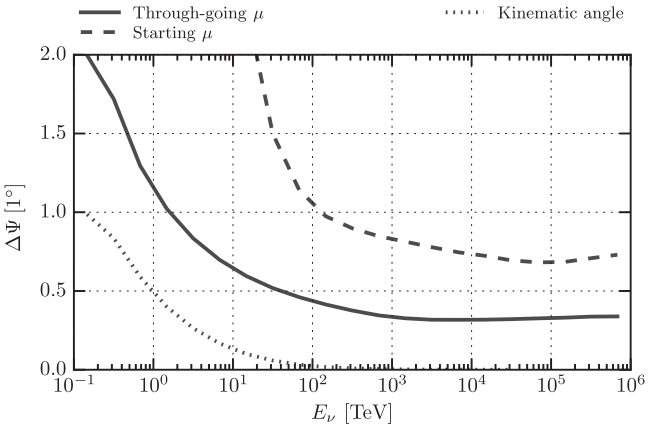

Figure 2. IceCube median angular resolution vs. neutrino energy for $\nu_\mu + \bar{\nu}_\mu$ calculated from Monte Carlo simulation for the IC86 sample described in Section 2.2. Through-going tracks (solid black) are shown together with starting tracks (dashed black; see Section 2.3). Moreover, the median kinematic angle of the secondary muon in CC neutrino interactions is shown (dotted black line).

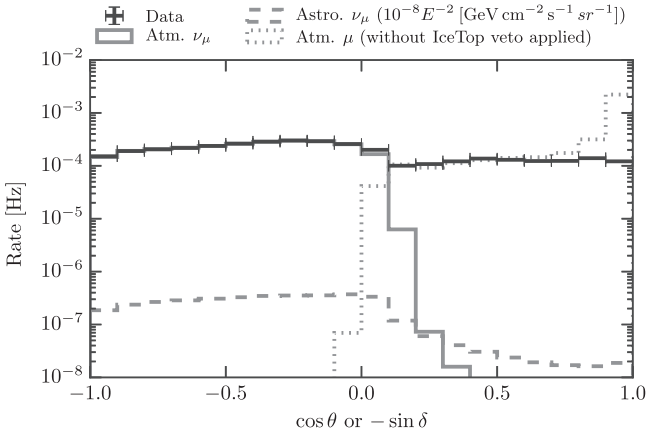

Figure 3. Zenith ($\cos\theta$) or declination ($-\sin\delta$) distribution of the through-going track sample after event selection (2012–2015 data). Values of -1 correspond to vertically up-going events. Shown is the experimental data (black), compared to the atmospheric $\nu_\mu + \bar{\nu}_\mu$ expectation of conventional atmospheric (solid gray) and astrophysical neutrinos (dashed gray), and atmospheric muons (dotted gray) from Monte Carlo simulation. For simulated atmospheric muons, the plot shows the distribution without the IceTop veto applied.

variables are used to further discriminate atmospheric muon bundles from single muons. These variables use the deposited energy along the track, as well as the light-arrival time of photons at the DOMs. The Cerenkov light yield for high-energy muons is dominated by stochastic cascades from energy losses along the track superimposed to the Cerenkov cone of the muon track. Bundles of muons at lower energies show less frequent losses by stochastic cascades. The result is a smoother light yield along the track. Furthermore, muon bundles consist of a superposition of many Cerenkov cones, resulting in many photons arriving earlier than under the assumption of one single Cerenkov cone. For a signal-spectrum E^{-2}, a BDT is trained for final selection of events. The large backgrounds require harsh cuts to reduce their rate significantly, resulting in an effective selection of only very high energy events, as shown in Figure 1 (yellow and purple). It is evident that the energy threshold in the down-going region increases to $\sim$100 TeV and even further for more vertically down-going events. The IceTop surface array is used as an active veto against coincident air-shower events for vertically down-going events. For high energies, this vetoes 90% of the events for vertically down-going events and less for inclined events, with random coincidences in less than 0.1% of the cases (Aartsen et al. 2013c); compare Figure 3. The final event rate in the southern sky is optimized to yield the best sensitivity and discovery potential for an E^{-2} spectrum.

The distribution of the cosine zenith $\cos\theta$ (equivalent to the negative sine of declination $-\sin\delta$ in equatorial coordinates) is shown in Figure 3. The event rate for experimental data of all 3 yr is compared to the expectations of muon neutrinos and atmospheric mouns estimated from Monte Carlo simulation. In the northern sky ($\theta > 85°$), the sample is dominated by atmospheric neutrinos produced in the decays of kaons and pions in cosmic-ray air showers (Honda et al. 2007) and is well described by Monte Carlo simulation. In the southern sky, the neutrino event rate reduces drastically due to the higher energy threshold mentioned before. Instead, atmospheric muons are the dominant component. Astrophysical neutrinos with hard energy spectra (as, e.g., shown with E^{-2}) do not suffer a rate loss as severe as for the soft energy spectrum of atmospheric neutrinos. For very vertically down-going events, the IceTop surface array vetoes atmospheric muon and neutrino events because of their coincident air shower. In this region, the observed event rate is kept constant with the rest of the southern sky using looser cuts on the BDT score, which allows more neutrinos to be detected especially at the lower energy end. Hence, the corresponding event rate in Figure 3 does not decrease above $\cos\theta > 0.7$.

2.3. Starting Tracks

In the southern sky, the large background of atmospheric muons reduces the efficiency to select through-going tracks induced by neutrinos below the PeV regime. A very large fraction of the aforementioned background can be rejected by imposing an active veto at the detector boundary, as, for example, used in Aartsen et al. (2013a). This reduces the detector volume to a smaller fraction of the instrumented volume sacrificing statistics for signal purity. Furthermore, the more clearly an event is identified as a starting track, the more probable it is to be an astrophysical rather than atmospheric background. Down-going atmospheric neutrino events at high energy are likely to be accompanied by muons produced in the same cosmic-ray shower that triggers the veto and reduces the atmospheric neutrino background (Schönert et al. 2009; Gaisser et al. 2014). In analyses using veto techniques (Aartsen et al. 2013a, 2015b), the selection is usually more efficient for cascade-like events than tracks, and high astrophysical neutrino purity demands neglecting energies below 60 TeV, where backgrounds are more abundant. In searches for point-like sources of astrophysical neutrinos, track-like events are of great importance given their good angular resolution compared to cascade-like events. Furthermore, the purity demands are lower since the signal of a point-like source is restricted to a small portion of the sky, hence reducing the background significantly. Consequently, the minimum required total charge deposited in the PMTs of the IceCube detector by an event is lowered to 1500 p.e. compared to 6000 p.e. (Aartsen et al. 2013a), resulting in a higher signal efficiency at lower energies. In addition, only down-going tracks are used, and cuts are imposed that select well-reconstructed track-like events (Aartsen et al. 2016a). For $\nu_\mu + \bar{\nu}_\mu$ events at energies smaller than 200 TeV, the effective area of the analysis is bigger than for vertically through-going tracks ($\delta < -30°$; Figure 1). For energies up to 1 PeV, the effective area is smaller, but a higher purity is achieved. The angular resolution for starting tracks is shown in Figure 2 (dashed) and is $\sim$1° in the interesting energy region; the reconstruction is worse than for through-going events (solid), due to a smaller lever arm for tracks starting within the fiducial volume of the detector.

In 5 yr, 961 events were recorded in the southern sky starting track sample. The overlap of events in the starting track sample and the through-going events is very small, and overlapping events are removed from the through-going sample because of its higher background rate.

3. Methods

In order to look for clustering in the sky, the analysis uses an unbinned likelihood maximization, similar to the previous analyses (Aartsen et al. 2014e). The unbinned likelihood is

defined as

$$\mathcal{L}(n_S, \gamma) = \prod_i \left(\frac{n_S}{N} \mathcal{S}(|\boldsymbol{x}_S - \boldsymbol{x}_i|, E_i; \gamma) + \left(1 - \frac{n_S}{N}\right) \mathcal{B}(\sin\delta_i, E_i) \right) \quad (2)$$

using multiple observables that are introduced in the following. The signal hypothesis used in this work assumes time-integrated emission of neutrinos. Hence, the signature reduces to spatial clustering modeled with a two-dimensional Gaussian $\exp(-|\boldsymbol{x}_S - \boldsymbol{x}_i|^2/2\sigma_i^2)/(2\pi\sigma_i^2)$ using the reconstruction uncertainty σ_i estimated on an event-by-event basis (Neunhöffer 2006; Abbasi et al. 2011). The probability distribution function for the spatial distribution of the background is estimated using experimental data and depends only on the event's declination δ_i, and the probability in right ascension is distributed uniformly, $1/2\pi$. This yields $\mathcal{P}_\mathcal{B}(\sin\delta_i)/2\pi$ for the spatial probability of the background.

In addition, energy information is used to distinguish background with soft spectra ($E^{-3.7}$) from signal with harder spectra of typically E^{-2}. Hence, for each event, probability distributions $\mathcal{E}_{\mathcal{S}/\mathcal{B}}(E_i)$ for signal and background are evaluated using the event's energy proxy E_i. For signal, an unbroken power law with variable index γ, $d\phi/dE_\nu \propto E^{-\gamma}$, is used, and the background is estimated from experimental data. The estimation is declination dependent, because of the energy dependence of the effective area (Figure 1). This yields the final modeling of probabilities for signal and background

$$\mathcal{S} = \frac{1}{2\pi\sigma_i^2} e^{-\frac{|\boldsymbol{x}_S - \boldsymbol{x}_i|^2}{2\sigma_i^2}} \times \mathcal{E}_\mathcal{S}(E_i, \sin\delta_i; \gamma)$$
$$\mathcal{B} = \frac{\mathcal{P}_\mathcal{B}(\sin\delta_i)}{2\pi} \times \mathcal{E}_\mathcal{B}(E_i, \sin\delta_i) \quad (3)$$

entering the unbinned likelihood calculation in Equation (2). Two parameters are fit in the likelihood, the number of source events $n_S \geqslant 0$ and the source spectral index $\gamma \in [1, 4]$.

In contrast to through-going tracks (Section 2.2), no declination dependence of the energy distribution is observed for starting tracks (Section 2.3). This is due to two reasons: the sample only uses down-going events so Earth absorption does not occur, and a uniform charge threshold over all declinations is applied, yielding a uniform effective area (Aartsen et al. 2016a). Meanwhile, starting tracks carry more information than direction and energy; for starting tracks, the vertex of a neutrino interaction can be reconstructed from the first visible light. A background of atmospheric muons can sneak past the veto by not emitting enough light prior to detection. Nevertheless, the higher the energy of the reconstructed track gets, the more likely it is for the vertex to be reconstructed close to the detector boundary, due to constant light emission along the track, as shown in Figure 4. A clear anticorrelation of event energy and *starting distance*[55] is observed for background events (blue). Truly starting signal neutrinos (red) do not show this correlation because the entering neutrino does not emit light. Consequently, the starting distance d_i can be used in addition to the event energy, to disentangle signal and background, modifying the energy likelihood $\mathcal{E}(E_i) \rightarrow \mathcal{E}(E_i, d_i)$, resulting in an additional discrimination power at lower energies.

[55] Distance along the track pointed back from the reconstructed vertex to the entry point in the detector; see Aartsen et al. (2016a) for more information.

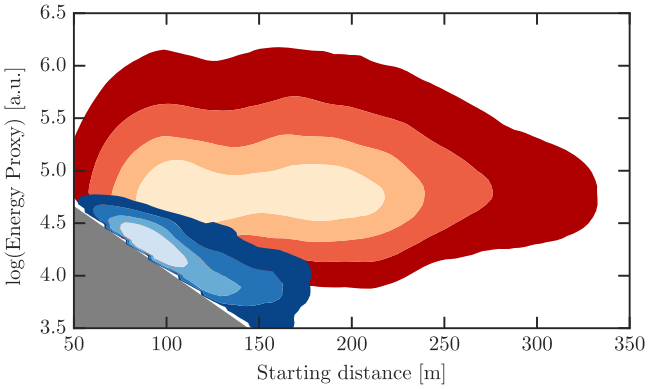

Figure 4. Probability distribution of starting distance vs. energy proxy (logarithmic, in arbitrary units, a.u.) for both atmospheric background (blue) and neutrinos (red) with E^{-2} spectrum. Different contours depict regions of 20% coverage each. The gray shaded area shows a region of no coverage resulting from a cut in the selection of Aartsen et al. (2016a).

As in the previous analysis (Aartsen et al. 2014e), the different samples listed in Table 1 consist of different detector configurations including partial detector configurations, plus samples using only starting tracks. The total likelihood of all combined samples is the product of all individual likelihoods, or the sum of the logarithms, $\log\mathcal{L}(n_S, \gamma) = \sum_j \log\mathcal{L}(n_S^j, \gamma)$ for all samples j. In the scenario of steady emission, the total number of signal events n_S is split proportionally among the samples given their exposure time and expected signal statistics derived from the effective area (Figure 1 and Equation (1)) and the value of the spectral index fitting parameter γ:

$$n_S^j = n_S \times \frac{\int_0^\infty dE\, A_{\rm eff}^j(E, \sin\delta) E^{-\gamma}}{\sum_i \int_0^\infty dE\, A_{\rm eff}^i(E, \sin\delta) E^{-\gamma}}. \quad (4)$$

Thus, the unbinned likelihood in Equation (2) is maximized using two parameters only for all samples, that is, the number of signal-like events n_S and the spectral index γ. The null hypothesis is the observation of no signal-like events $n_S = 0$ and defines the test statistic of best-fitting hypothesis $(\hat{n}_S, \hat{\gamma})$ over null hypothesis, $\mathcal{TS} = 2\log(\mathcal{L}(\hat{n}_S, \hat{\gamma})/\mathcal{L}(n_S = 0))$. In the maximization of the test statistic, only overfluctuations $n_S \geqslant 0$ are taken into account; negative n_S are not part of the physics scenario of neutrino sources (Braun et al. 2008) and are not considered here. Thus, the test statistic of the null hypothesis is expected to split into two fractions, one bound at $n_S = 0$ and overfluctuations $n_S > 0$. The latter are distributed according to $\chi^2_{n_{\rm dof}}$-statistics with $n_{\rm dof} \sim 1.5$, less than the number of free parameters (2). This is due to n_S and γ being partly degenerate; moreover, γ is only defined for $n_S > 0$, as can be seen in Equation (2). The fraction η of overfluctuations ranges from 50% to 30% in the northern and southern sky, respectively. From the estimation of the test statistic distribution, the p-value $p = \eta \times \int_{\mathcal{TS}}^\infty dX\, \chi^2(X\,|n_{\rm dof})$ of an observation being consistent with background can be calculated. The p-value will mostly be quoted as $-\log_{10} p$ in the following.

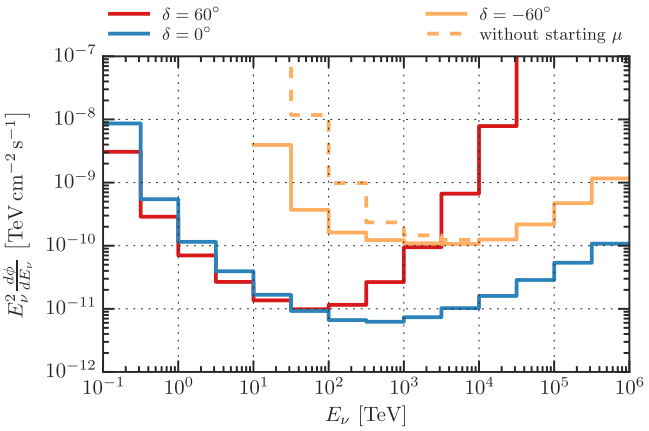

Figure 5. Discovery potential (5σ) for this analysis in different bins of neutrino energy E_ν with half-decade width. Within this energy range, an E_ν^{-2} spectrum is used. Three different declinations are shown: up-going (red, $\delta = 60°$), horizontal (blue, $\delta = 0°$), and down-going (yellow, $\delta = -60°$) events. For down-going events, the dashed line shows the discovery potential *not using* the starting track sample described in Section 2.3.

3.1. Neutrino Point-source Sensitivity

Figure 5 shows the 5σ discovery potential of the unbinned likelihood analysis versus neutrino energy for point sources at various declinations.[56] A $\nu_\mu + \bar{\nu}_\mu$ neutrino signal with half-decade width is used for signal injection, using an E^{-2} spectrum within the energy range indicated by the step function. The discovery potential shows a strong variation with declination. In the up-going region ($\delta \geqslant -5°$), atmospheric muon background is efficiently removed and a large effective area with good angular resolution is achieved above TeV energies; compare Figures 1 and 2. This yields a discovery potential reaching from TeV to EeV energies at the horizon ($\delta = 0°$, blue). For vertically up-going events ($\delta = 60°$, red), neutrinos at energies above 100 TeV begin to be absorbed in Earth, hence reducing the discovery potential compared to the horizon.

In the down-going region (southern sky, $\delta < -5°$), large backgrounds of atmospheric muons result in a higher energy threshold of $\sim$100 TeV. Moreover, muon bundles imitate single muons at very high energies, resulting in a high-energy background. This diminishes the performance compared to the northern sky. At $\delta = -60°$ (yellow), the discovery potential is most effective above energies of 100 TeV; in fact, in between 100 TeV and PeV energies, starting tracks described in Section 2.3 dominate the sensitivity compared with through-going muons (Section 2.2). Even though the effective area is of the same order in this energy regime, starting tracks have significantly less background and thus a $\sim$170$\times$ higher purity (0.09 d^{-1} sr^{-1} background events for starting tracks compared to 15.5 d^{-1} sr^{-1} for through-going tracks). Including starting tracks gives a factor of $\sim$8 improvement in discovery potential at 100 TeV compared to only using through-going events (dashed yellow in Figure 5). In the southern sky, similar searches of Adrian-Martinez et al. (2014) test much lower energies, resulting in complementary results combined in Adrian-Martinez et al. (2015).

[56] The discovery potential is defined as a *false-positive* rate of 5σ or 2.87×10^{-7} with *false-negative* of 50%. The sensitivity is defined as a *false-positive* rate of 50% with *false-negative* of 10%.

3.2. Full-sky Search

To find the most significant clustering in the sky, the unbinned likelihood maximization is performed on the entire sky. This is done iteratively using a grid with isotropically spaced points (Gorski et al. 2005) finer than the typical event reconstruction uncertainty that enters the likelihood description in Equation (3).

Thus, for any point in the sky, the best-fitting $\hat{n}_S$, $\hat{\gamma}$, and the test statistic $\mathcal{TS}$ are obtained. The direction with the smallest p-value defines a *hot spot* showing the biggest deviation from background expectation. This is done for northern and southern sky separately, as they differ in atmospheric backgrounds and energy reach. Thus, two positions in the sky will be reported in the full-sky scan. The significance is trial corrected, accounting for the chance of background fluctuations occurring at any position in the sky. The probability to observe no pre-trial $\log_{10} p$ that is smaller than the one at the *hot spot* for N independent trials is given by

$$d\mathcal{P} = N\,(1 - p)^{N-1}\,dp. \tag{5}$$

For both northern and southern sky, the effective number of independent trials N in the sky is fitted to $\sim$190,000 by repeating the analysis on scrambled data maps. Regions close to the poles (5°) are excluded from the scan because no large off-source regions are available for scrambling. Accounting for the trial factor, a pre-trial significance of 5.67σ (p-value 7.13×10^{-9}) is needed for a *hot spot* to be detected at 3σ significance in the scan of the full sky.

3.3. Hot Spot Population Analysis

The large trial factor of the full-sky scan requires very strong sources that overcome the trial factor. Thus, in addition to looking at only the most significant spot in the sky, the entire sky can be tested for an accumulation of multiple spots at intermediate significance that exceeds the number expected by background.

From the scan of the full sky, the positions of all the local maxima exceeding $-\log_{10} p \geqslant 3$ are selected. The number of spots observed above a threshold of $-\log_{10} p_{\min}$ is compared to the background expectation from repeating the analysis on scrambled data maps. The threshold value is optimized to give the most significant excess over the mean background expectation $\lambda(-\log_{10} p_{\min})$ with Poisson statistics. The p-value of the observation of at least n spots, given this expectation, is

$$\mathcal{P} = e^{-\lambda} \sum_{m=n}^{\infty} \frac{\lambda^m}{m!} \tag{6}$$

and defines the test statistic of this test. Due to the optimization of the threshold $-\log_{10} p_{\min}$ to minimize $\mathcal{P}$, the final result is trial corrected using scrambled experimental data. This is done separately for northern and southern sky. In addition, parts of the sky coinciding with the Galactic plane $\pm 15°$ are analyzed as well for a Galactic contribution.

3.4. Source List Searches

In addition to the previously explained searches that did not make any prior assumptions regarding directions in the sky, sources of high-energy γ-rays can be used to search for neutrino emission. Thus, the trial factor of the unbiased full-sky scan can be effectively reduced by probing 74 promising

Table 2
Sources Contained in the First Source List

Type	Source	α 1°	δ 1°	p-value	n_S	γ	B_{1°	$\Phi^{90\%}_{\nu_\mu+\bar{\nu}_\mu}$ ζ[a]
BL Lac	PKS 0537-441	84.71	−44.09	⋯	0.0	⋯	45.7	9.79
	PKS 2155-304	329.72	−30.23	⋯	0.0	⋯	52.6	6.07
	PKS 0235+164	39.66	16.62	0.12	16.2	3.4	72.0	0.94
	1ES 0229+200	38.20	20.29	0.20	9.5	3.5	66.6	0.84
	W Comae	185.38	28.23	⋯	0.0	⋯	60.8	0.62
	Mrk 421	166.11	38.21	0.32	2.7	1.8	53.1	0.94
	Mrk 501	253.47	39.76	0.18	10.5	4.0	52.0	1.15
	BL Lac	330.68	42.28	⋯	0.0	⋯	50.4	0.63
	H1426+428	217.14	42.67	⋯	0.0	⋯	50.9	0.70
	3C 66A	35.67	43.04	⋯	0.0	⋯	50.9	0.70
	1ES 2344+514	356.77	51.70	⋯	0.0	⋯	46.3	0.81
	1ES 1959+650	300.00	65.15	0.018[b]	15.4	3.1	42.8	2.36
	S5 0716+71	110.47	71.34	⋯	0.0	⋯	38.4	1.34
Flat-spectrum	PKS 1454-354	224.36	−35.65	⋯	0.0	⋯	49.1	7.99
radio quasar	PKS 1622-297	246.53	−29.86	0.11	3.8	2.3	52.7	8.20
	QSO 1730-130	263.26	−13.08	⋯	0.0	⋯	49.8	2.18
	PKS 1406-076	212.24	−7.87	0.053[c]	7.3	2.6	50.5	1.65
	QSO 2022-077	306.42	−7.64	⋯	0.0	⋯	50.5	0.99
	3C 279	194.05	−5.79	0.42	0.5	2.0	54.3	0.63
	3C 273	187.28	2.05	0.25	7.7	3.2	76.4	0.59
	PKS 1502+106	226.10	10.49	0.38	3.1	2.7	73.7	0.59
	PKS 0528+134	82.73	13.53	0.44	2.7	4.0	73.0	0.60
	3C 454.3	343.49	16.15	0.12	4.1	2.0	72.3	0.93
	4C 38.41	248.81	38.13	0.12	6.3	2.4	53.2	1.31
Galactic center	Sgr A*	266.42	−29.01	⋯	0.0	⋯	52.2	6.08
Not identified	MGRO J1908+06	286.98	6.27	0.025	4.5	2.0	74.9	0.99
Pulsar wind	Geminga	98.48	17.77	⋯	0.0	⋯	69.3	0.49
nebula	Crab Nebula	83.63	22.01	0.34	6.1	3.8	67.0	0.68
	MGRO J2019+37	305.22	36.83	0.23	7.8	4.0	53.2	1.04
Star formation region	Cyg OB2	308.30	41.32	0.26	5.9	4.0	50.6	0.99
Supernova remnant	IC443	94.21	22.50	0.22	8.1	4.0	66.0	0.83
	Cas A	350.81	58.81	0.14	8.1	4.0	44.5	1.49
	TYCHO	6.36	64.18	0.27	4.6	3.4	42.4	1.23
Starburst/radio	Cen A	201.37	−43.02	0.21	0.5	1.2	46.2	10.41
galaxy	M87	187.71	12.39	⋯	0.0	⋯	73.2	0.48
	3C 123.0	69.27	29.67	⋯	0.0	⋯	59.5	0.57
	Cyg A	299.87	40.73	0.068	2.1	1.4	51.1	1.50
	NGC 1275	49.95	41.51	⋯	0.0	⋯	50.6	0.71
	M82	148.97	69.68	⋯	0.0	⋯	39.7	1.09
HMXB/mqso	SS 433	287.96	4.98	0.40	4.1	4.0	75.8	0.47
	HESS J0632+057	98.24	5.81	0.10	13.6	3.6	75.4	0.77
	Cyg X-1	299.59	35.20	0.31	4.5	4.0	54.4	0.90
	Cyg X-3	308.11	40.96	0.077	12.8	4.0	51.3	1.53
	LSI 303	40.13	61.23	⋯	0.0	⋯	43.8	0.79

Notes. Sources of the list are grouped by their classification and ordered in ascending declination δ. High-mass X-ray binaries and micro-quasars are abbreviated by *HMXB/mqso*. Spectral indices quoted as $\gamma = 4.0$ are at the boundary of the parameter space for minimization. This can happen when there is an overfluctuation of low-energy events close to the source location. It was ensured that for all events, the minimization converged successfully to the minimum within the parameter space. In addition to its type, common name, and coordinates (Equatorial (J2000)), the best fits of signal events n_S and spectral index γ with the pre-trial p-value $-\log_{10} p$ are quoted. For null observations $n_S = 0$, no p-value and spectral index are quoted. A 90% upper limit for an E^{-2} unbroken power law is calculated for all sources that showed clustering of neutrinos. The upper limits are shown in Figure 8; for null fits the limit equals the sensitivity of this analysis at the corresponding declination.
[a] Upper limits are in units of $\zeta = 10^{-12}\,\mathrm{TeV\,cm^{-2}\,s^{-1}}$.
[b] Most significant source in northern sky in this table. The trial-corrected p-value is 54%.
[c] Most significant source in southern sky in this table. The trial-corrected p-value is 37%.

sources selected a priori. The sources are collected in two lists as used in Aartsen et al. (2014e) and Adrian-Martinez et al. (2014), Aartsen et al. (2016a), respectively. The first one (44 sources) probes mainly the northern sky (34 candidates), and the largest fraction of sources are extragalactic objects. The list can be found in Table 2. The second list (Table 3) of 30 candidates focuses on the southern sky, especially Galactic sources.

The most significant source in each list will be trial corrected given the number of sources. For the first list, this procedure will be done separately for northern and southern sky. Hence, three post-trial p-values are reported.

Table 3
Sources Contained in the Second Source List, Using Only Sources in the Southern Sky and Focusing on Galactic Objects

Type	Source	α 1°	δ 1°	p-value	n_S	γ	B_{1°	$\Phi^{90\%}_{\nu_\mu+\bar{\nu}_\mu}$ ζ[a]
BL Lac	PKS 2005-489	302.37	−48.82	0.071	0.9	1.0	44.7	13.45
	PKS 0426-380	67.17	−37.93	⋯	0.0	⋯	47.2	8.93
	PKS 0548-322	87.67	−32.27	⋯	0.0	⋯	51.2	6.79
	H2356-309	359.78	−30.63	⋯	0.0	⋯	52.1	6.18
	1ES 1101-232	165.91	−23.49	⋯	0.0	⋯	52.6	4.64
	1ES 0347-121	57.35	−11.99	0.21	1.4	2.4	52.2	2.16
Flat-spectrum	PKS 0454-234	74.27	−23.43	⋯	0.0	⋯	52.8	4.58
radio quasar	PKS 0727-11	112.58	−11.70	0.20	2.7	3.7	52.0	2.30
Not identified	HESS J1507-622	226.72	−62.34	⋯	0.0	⋯	43.4	11.02
	HESS J1503-582	226.46	−58.74	⋯	0.0	⋯	45.5	11.79
	HESS J1741-302	265.25	−30.20	0.19	2.1	4.0	52.6	7.33
	HESS J1834-087	278.69	−8.76	0.21	1.2	3.7	49.5	1.47
Pulsar wind	HESS J1356-645	209.00	−64.50	⋯	0.0	⋯	42.4	10.90
nebula	PSR B1259-63	197.55	−63.52	0.21	1.3	2.0	42.7	11.43
	HESS J1303-631	195.74	−63.20	0.076	4.5	2.3	42.3	13.61
	MSH 15-52	228.53	−59.16	⋯	0.0	⋯	44.9	11.28
	HESS J1023-575	155.83	−57.76	⋯	0.0	⋯	46.4	11.79
	HESS J1616-508	243.78	−51.40	0.0022[b]	2.4	4.0	45.0	19.37
	HESS J1632-478	248.04	−47.82	0.16	1.5	2.7	44.7	10.79
	Vela X	128.75	−45.60	0.13	2.7	2.4	45.8	10.79
	HESS J1837-069	279.41	−6.95	⋯	0.0	⋯	48.1	0.89
Supernova remnant	RCW 86	220.68	−62.48	⋯	0.0	⋯	43.1	11.02
	RX J0852.0-4622	133.00	−46.37	⋯	0.0	⋯	45.6	10.40
	RX J1713.7-3946	258.25	−39.75	⋯	0.0	⋯	45.5	9.22
	W28	270.43	−23.34	⋯	0.0	⋯	52.9	4.58
Seyfert galaxy	ESO 139-G12	264.41	−59.94	⋯	0.0	⋯	44.0	11.28
HMXB/mqso	Cir X-1	230.17	−57.17	⋯	0.0	⋯	46.3	11.03
	GX 339-4	255.70	−48.79	0.15	2.6	2.2	44.8	11.29
	LS 5039	276.56	−14.83	0.26	2.1	4.0	52.3	2.72
Massive star cluster	HESS J1614-518	243.58	−51.82	0.0058	2.2	4.0	45.4	18.33

Notes. Please refer to Table 2 for comments regarding this table.
The information listed is the same as in Table 2.
[a] Upper limits are in units of $\zeta = 10^{-12}$ TeV cm^{-2} s^{-1}.
[b] Most significant source in this table (south only). The trial-corrected p-value is 9.3%.

3.5. Systematic Uncertainties

All analyses described in the previous sections are robust against systematic uncertainties. Background is estimated using experimental data that are scrambled in right ascension and does not require dedicated Monte Carlo simulation. For the calculation of neutrino fluxes, however, Monte Carlo simulation is needed to insert neutrino sources into background maps. The resulting neutrino fluxes are affected by systematic uncertainties. Especially, the evaluation of the effective area and reconstruction performance is affected by systematic effects in Monte Carlo, and thus the sensitivity to neutrino fluxes (Equation (1)). Main systematic uncertainties include the optical properties (scattering, absorption) of the South Pole ice (Aartsen et al. 2013b), the optical efficiency of Cerenkov light production yield and detection in the DOMs (Abbasi et al. 2010), and different photo-nuclear interaction models (Abramowicz et al. 1991; Abramowicz & Levy 1997; Bugaev & Shlepin 2003a, 2003b). All systematic effects are propagated through the entire likelihood analysis described in Section 3 to obtain the uncertainties on the fluxes using $d\phi/dE_\nu \propto E^{-2}$ spectra. The biggest impact on the fluxes comes from varying the optical efficiency by ±10%, resulting in a flux uncertainty of 7.5%. Increasing the absorption or scattering of photons in ice by 10% affects the flux by 5.6%. Uncertainties in the photo-nuclear cross sections (Bugaev & Shlepin 2003a, 2003b) result in a flux uncertainty of similar size with 5.9%. Adding these values in quadrature yields a total systematic uncertainty of 11% on $\nu_\mu + \bar{\nu}_\mu$ fluxes quoted in the following.

For all locations tested, only the maximal likelihood values of $\hat{n}_S$ and $\hat{\gamma}$ are reported. Because of small event statistics at the position of the likelihood maximization and limited energy resolution of the neutrino energy (compare Section 2.2), uncertainties on the spectral index are of the order of ±1 and reduce to ±0.5 for values of n_S of ∼15 and ∼50, respectively (Braun et al. 2008). Hence, the impact of systematic uncertainties in the energy reconstruction is small compared to the statistical limitations.

Albeit not a systematic uncertainty per se, so far only fluxes of $\nu_\mu + \bar{\nu}_\mu$ were considered. This is a conservative estimate, because track-like events can also originate in other cases that are discussed in the following. First, tau leptons created in charged-current $\nu_\tau + \bar{\nu}_\tau$ interactions decay into muons with a 17% branching ratio (Jeong & Reno 2010; Olive et al. 2014), resulting in a muon track with lower energy due to the three-body decay $\tau \rightarrow \mu\nu_\mu\nu_\tau$. This decay is important for up-going events, because secondary neutrinos are produced in τ-neutrino regeneration during propagation. Second, interactions of $\bar{\nu}_e + e^- \rightarrow W^-$ at the Glashow resonance (Glashow 1960) at 6.3 PeV produce tracks ($\bar{\nu}_e + e^- \rightarrow \bar{\nu}_\mu + \mu^-$) at the 10.6%

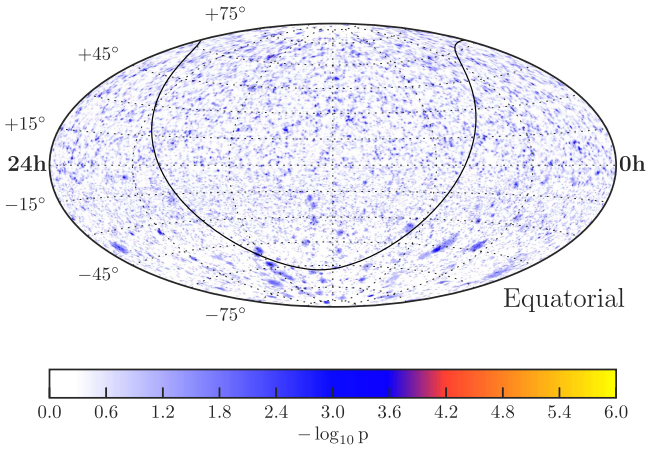

Figure 6. All-sky result of the unbinned likelihood maximization shown in equatorial coordinates (J2000). Shown is the negative logarithm of the pre-trial p-value, $-\log_{10} p$, assuming no clustering as the null hypothesis. The Galactic plane is shown as the black line.

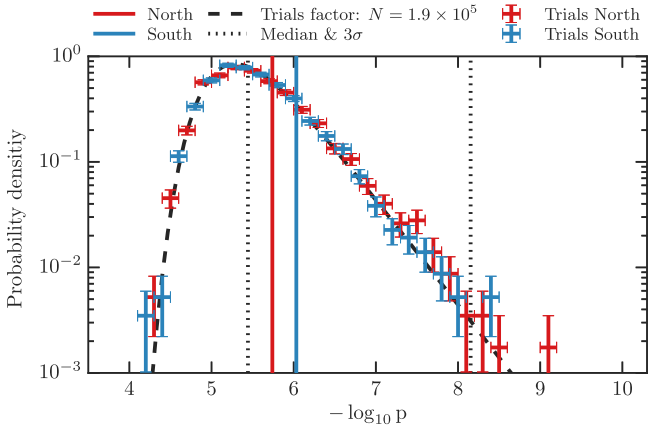

Figure 7. Trial correction of the most significant spots in the sky that were observed in the 7 yr search. Solid vertical lines indicate the pre-trial p-value of the most significant spots in each half of the sky; crosses show the distribution of spots similarly obtained in scrambled data trials. The trials are modeled by an analytic parameterization of the trial correction (Equation (5), black dashed line) that corresponds to 1.9×10^5 independent trials per half of the sky.

branching ratio (Olive et al. 2014). Lastly, at the highest energies above PeV, τ-neutrino-induced double bangs are well reconstructable and further increase the number of τ-flavored events in the sample. Accounting for these fluxes assuming an equal flavor ratio at Earth reduces the per-flavor flux necessary for detection by 5% assuming an unbroken E^{-2} spectrum. For harder spectra, the sensitivity gain due to regeneration effects in the northern sky becomes stronger. For example, a spectrum of $d\phi/dE_\nu \propto E^{-1}$ has a 30% improved sensitivity compared to only considering muon neutrinos. This greatly increases the sensitivity with respect to models that predict very hard neutrino energy spectra peaking above PeV energies (Petropoulou et al. 2015; Reimer 2015).

4. Results and Implications

In the unbinned likelihood analysis using 7 yr of IceCube livetime, no significant excess of astrophysical neutrino sources was found. In the following, the results of the three tests introduced in the previous sections are discussed and 90% upper limits on neutrino source fluxes are calculated. Finally, implications with respect to neutrino models of γ-ray sources and the observed diffuse neutrino flux are presented.

4.1. All-sky Scan

Figure 6 depicts the pre-trial p-value $-\log_{10} p$ of all points in the sky in equatorial coordinates (J2000) with respect to the null hypothesis of no observed clustering.

In the northern sky, the most significant position was at $\alpha = 32.^\circ2$, $\delta = 62.^\circ1$ at an accuracy of $0.^\circ35$ ($0.^\circ5$) for 1σ (90%) contours using Wilks's theorem with two degrees of freedom. The best-fit parameters at the location are $\hat{n}_S = 32.6$ and $\hat{\gamma} = 2.8$, yielding a pre-trial p-value of 1.82×10^{-6}. Looking at each of the combined seasons individually reveals that for each season clustering is observed, providing no indication of time dependence that could suggest additional evidence for an astrophysical origin.

In the southern sky, the most significant point is at $\alpha = 174.^\circ6$, $\delta = -39.^\circ3$. The best-fit point is at $\hat{n}_S = 15.4$, with spectral index $\hat{\gamma} = 2.9$. The uncertainty of the location amounts to $0.^\circ22$ ($0.^\circ32$) for 1σ (90%). The pre-trial p-value is 0.93×10^{-6}; most of the significance at this location is shared by the newly added data of through-going and starting tracks. Indeed, one starting track is within $0.^\circ9$ distance to the location, which is within 1σ of its reconstruction uncertainty.

Due to the large number of tested locations in the sky, the two most significant locations in the sky have to be trial corrected with the trial correction in Equation (5) that is estimated by repeating the full-sky scan on scrambled data trials, as shown in Figure 7. This yields post-trial p-values of 29% and 17% for northern and southern sky, respectively. Hence, the full-sky results are in agreement with a pure background assumption, and no significant clustering is observed. For an unbroken E^{-2} power-law spectrum, the 90% upper limits of the two most significant positions are $E_\nu^2 d\phi/dE_\nu = 4.49 \times 10^{-12}$ TeV cm^{-2} s^{-1} in the northern sky and $E_\nu^2 d\phi/dE_\nu = 2.92 \times 10^{-11}$ TeV cm^{-2} s^{-1} in the southern sky. For softer spectra of E^{-3}, the 90% upper limits yield $E^3 d\phi/dE_\nu = 5.08 \times 10^{-11}$ TeV^2 cm^{-2} s^{-1} and $E^3 d\phi/dE_\nu = 1.29 \times 10^{-8}$ TeV^2 cm^{-2} s^{-1} for the northern and southern spot, respectively. In Figure 8, the solid blue line indicates the 90% upper limit established by the hottest spot results. A neutrino source at any declination δ that would emit a steady flux higher than this curve would be detected 90% of the time as having a greater significance than that actually observed for the hottest spots found in the analysis (whose 90% upper limits are highlighted as stars on the blue line).

Besides the results of the full-sky scan, there are two neutrino events detected with IceCube that are worth commenting on here. The first one is the highest energetic neutrino event detected (4.5 ± 1.2 PeV) so far with IceCube (Schoenen & Rädel 2015; Aartsen et al. 2016b), a neutrino-induced up-going muon track with very precise angular resolution. This neutrino event is part of the through-going track sample (Section 2.2). At its position ($\alpha = 110^\circ$, $\delta = 11.^\circ5$), no significant clustering is observed (pre-trial 5.2%). A slight excess is indeed observed, but originates from the PeV event alone. The second interesting event is a straight down-going starting track at 430 TeV deposited energy (Aartsen et al. 2015f). Not only does it start inside of the IceCube detector, but the reconstructed track points back to the IceTop surface detector, and no atmospheric shower is observed in coincidence with the event. This event is part of the starting

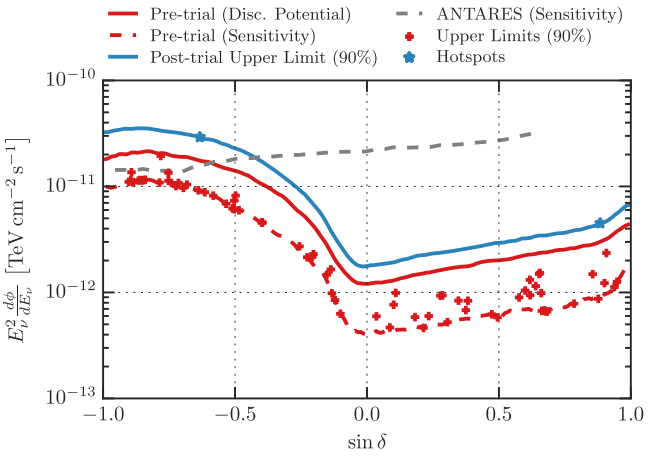

Figure 8. Discovery potential (5σ, solid red) and sensitivity (dashed red) for a $\nu_\mu + \bar{\nu}_\mu$ unbroken $E_\nu^2 d\phi/dE_\nu$ flux shown against declination δ. The gray line shows the results of Adrian-Martinez et al. (2014) in the south. Upper limits of source candidates in Table 2 and Table 3 are depicted by red crosses. The blue line represents the upper limit for the observed most significant spots in each half of the sky for all declinations; the actual declination position of the spots is indicated by a star.

track sample (Section 2.3), but no clustering of events apart from the track itself is observed at the location in the sky ($\alpha = 218°$, $\delta = -86°$), and the pre-trial p-value is 0.6%.

4.2. Hot Spot Population

The search for populations of weak sources in the full sky in Figure 6 did not reveal any significant outcome above the background expectation. In Figure 9, the number of spots versus pre-trial p-value $-\log_{10} p_{\min}$ threshold is shown for northern (left) and southern sky (right). The observed number of spots is shown versus background expectation, with shaded areas indicating 1σ, 2σ, and 3σ intervals. This is then converted to a *local* p-value $\mathcal{P}$ according to Equation (6).

In the northern sky, the most significant excess is observed above a threshold of $-\log_{10} p_{\min} \geqslant 3.35$, with 72 spots above a scrambled data expectation of 56.7. The local p-value of such an excess is $\mathcal{P} = 2.8\%$ and increases to 25% after trial correction. For the southern sky, seven spots above an expectation of 2.1 spots at $-\log_{10} p_{\min} \geqslant 4.66$ are reported. The probability of this happening by fluctuations of background is 0.62%. After correcting this for trials by scanning in $-\log_{10} p_{\min}$ for the biggest excess, the p-value increases to 8.2%. Restricting the analysis only to regions within $\pm 15°$ of the Galactic plane, the biggest excess is observed at $-\log_{10} p_{\min} \geqslant 5.68$, corresponding to a single spot, which is also the same spot that was most significant in the northern hemisphere full sky scan. The background expectation is 0.04, giving a local p-value of 3.8% that increases to 26% after trial correction.

Consequently, in both hemispheres and the Galactic plane, no significant population of sources over background expectation was found. Figure 10 shows the sensitivity, 5σ discovery potential, and 90% upper limit for northern (left) and southern sky (right). This is shown against an increasing number of sources, where each source is assumed to be of equal luminosity with an unbroken E^{-2} spectrum. The flux value is averaged over all declinations of the corresponding half of the sky. By comparing this to a scenario where all of the observed diffuse astrophysical neutrino flux (Aartsen et al. 2014c) $E_\nu^2 d\phi/dE_\nu \sim 10^{-11}$ TeV cm^{-2} s^{-1} sr^{-1} is shared equally among N_{Sources} in the sky, in the northern sky, the analysis result excludes populations of 1000 or fewer equal-strength sources, whereas in the south, the result only excludes populations of 40 or fewer equal-strength sources of the astrophysical flux.

4.3. Source List Candidates

In Tables 2 and 3, the fit results of the two source lists are quoted. For each source, the fit parameters $\hat{n}_S$ and $\hat{\gamma}$ are quoted. Furthermore, the pre-trial p-value and the mean number of background events $B_{1°}$ within a 1° circle around the source are listed. For each source, 90% upper limits are calculated using an unbroken E^{-2} spectrum. The upper limits are shown as red crosses in Figure 8 at the corresponding declination of the source.

In the first source list, the sources most significant are the blazar 1ES 1959+650 and flat-spectrum radio quasar (FSRQ) PKS 1406-076 in the northern and southern sky, respectively. At the position of 1ES 1959+650 the pre-trial p-value is 1.8%, with best-fit parameters $\hat{n}_S = 15.4$ and $\hat{\gamma} = 3.1$. The resulting 90% upper limit for an unbroken E^{-2} $\nu_\mu + \bar{\nu}_\mu$ flux of the observed p-value at declination $\delta = 65.^\circ 15$ of 1ES 1959+650 yields $E_\nu^2 d\phi/dE_\nu = 2.36 \times 10^{-12}$ TeV cm^{-2} s^{-1}. For PKS 1406-076 at $\delta = -7.^\circ 87$, the pre-trial p-value of 5.3% with $\hat{n}_S = 7.3$ and $\hat{\gamma} = 2.6$ results in a 90% upper limit of $E_\nu^2 d\phi/dE_\nu = 1.65 \times 10^{-12}$ TeV cm^{-2} s^{-1}. For trial correction, the source list is split into a northern and a southern part, with the division at $\delta = -5°$. The size of the source list is then 34 (10) and yields a trial-corrected p-value of 54% (37%) for the northern sky (southern sky). Hence, the results of the first source list are in agreement with the background expectation.

In the second source list, the most significant source is HESS J1616-508. The fit values $\hat{n}_S = 2.4$ and $\hat{\gamma} = 4.0$ result in a pre-trial p-value of 0.22%. The 90% upper limit is $E_\nu^2 d\phi/dE_\nu = 1.94 \times 10^{-11}$ TeV cm^{-2} s^{-1}. Trial correction with all 30 sources of the list yields a post-trial p-value of 9.3%. Most of the significance at the position of HESS J1616-508 comes from one starting track only $0.^\circ 34$ away, while no significant clustering of high-energy events is observed in the through-going event samples. Starting tracks access lower energies in the southern sky (see Figures 1, 5). As explained in Equation (4), the number of source-like neutrinos n_S is distributed among the different samples according to their signal expectation for a spectral index γ. Consequently, if the clustering is only observed in starting tracks, soft spectral indices at the boundary $\hat{\gamma} = 4$ are preferred as they give more weight to the starting track sample that is most efficient for soft spectra compared to through-going track samples in the southern sky.

In conclusion, both of the two source lists show no significant evidence for clustering of astrophysical neutrinos, and all results are consistent with background.

4.4. Multiwavelength Model Constraints

Above, upper limits on neutrino emission from sources were made using unbroken $d\phi/dE_\nu \propto E^{-2}$ fluxes as a benchmark. However, more specific estimates for neutrino fluxes can be made using multiwavelength data of γ-ray sources. In decays of pions, both γ-rays and neutrinos are produced (Anchordoqui

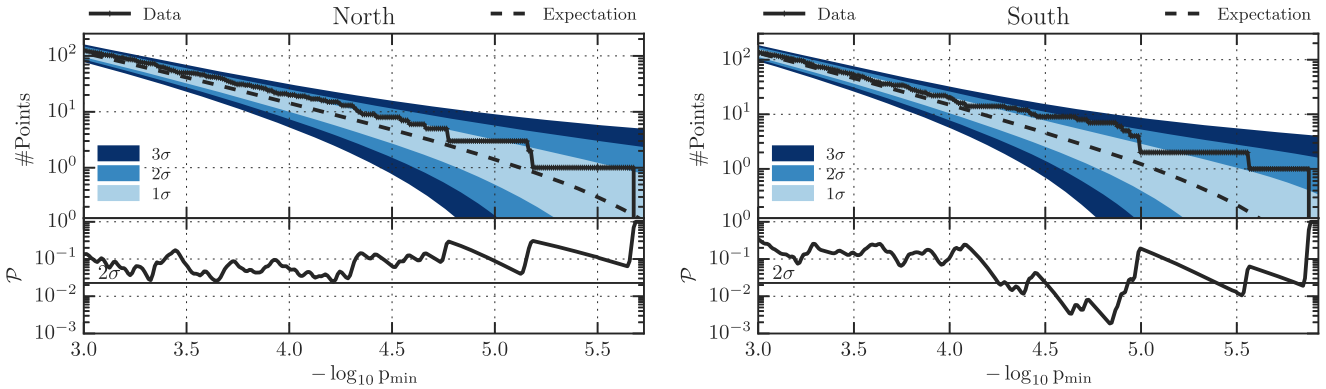

Figure 9. Number of associated spots observed with a minimum pre-trial p-value of $-\log_{10} p_{\rm min}$ of the unbinned likelihood fit in the northern (left) and southern sky (right), respectively. The top plots show the number of spots (solid black) in comparison to background expectation (dashed black) with confidence intervals of one, two, and three standard deviations shown as shaded blue areas. The points on the far right end of the x-axis correspond to the hottest spots observed in the northern and southern sky. The bottom plots show the local p-value $\mathcal{P}$ (Equation (6)) of observing X events given the background mean expectation of Y using Poissonian statistics.

et al. 2014). Due to long-baseline oscillations, any flavor composition at the source will result in a sizable fraction of muon neutrinos at Earth (Athar et al. 2006). Due to no significant observation of clustering, upper limits on specific models are set by injecting signal events at the corresponding source declination according to the energy spectrum $E_\nu^2 d\phi/dE_\nu$ given by the model.

The first source considered is the Crab Nebula, a pulsar wind nebula, and the strongest steady TeV γ-ray source in the sky. At a declination of $\delta = 22°$, it is in the region where IceCube covers a wide range of energies efficiently; compare Figure 5. Two scenarios of neutrino emission from this source are considered. Figure 11 shows the neutrino emission (thin line) with respect to the 90% upper limit (thick line) of IceCube. At the position of the Crab Nebula, an overfluctuation with p-value 34% is observed, which results in an upper limit higher than IceCube's potential sensitivity (dashed). By convoluting the differential discovery potential (Figure 5) at the source position and the model neutrino spectrum, the energy region, where 90% of the constraining power of IceCube originates, for a specific model is calculated. This is indicated by the energy region where the limits and sensitivities are drawn in Figure 11 for each of the following models.

Regarding the Crab Nebula, the first model taken into account (red in Figure 11) is by Amato et al. (2003) and uses inelastic p–p scattering at the source to model the neutrino emission where 60% of the wind luminosity $L_{\rm tot}$ is carried by protons. The model shown is for a Lorentz factor of the wind of $\Gamma = 10^7$, where the energy density peaks at ∼500 TeV and assumes a target density of

$$n_t = 10\mu\,(M_{N\odot}/R_{\rm pc}^3)\ {\rm cm}^{-3} \tag{7}$$

with $\mu = 20$ (shown in Figure 11) as defined in Equation (9) in Amato et al. (2003). $M_{N\odot}$ and $R_{\rm pc}$ are the mass of the supernova ejecta contained in filamentary structures within the nebula and its radius, respectively. With the increased statistics compared to the previous analysis (Aartsen et al. 2014e), the 90% upper limit now surpasses the prediction of $\mu = 20$, hence constraining the target density $\mu^{90\%} < 12$. Upper limits on μ and the proton wind luminosity $L_{\rm p}$ in units of the total wind luminosity $L_{\rm tot}$ for lower values of the Lorentz wind Γ are shown in Figure 12. Lower values of Γ shift the neutrino energy spectrum to lower energies into the TeV region where IceCube is most sensitive in the northern hemisphere. Hence, target densities $\mu < 20$ as mentioned in Atoyan & Aharonian (1996) are partially constrained by IceCube for a proton luminosity fraction of 60%. For $\Gamma = 10^5$, the sensitivity is at the level of $\mu = 5$ corresponding to a uniform mass distribution in the nebula as pointed out by Amato et al. (2003). For Lorentz wind factors $\Gamma < 10^6$, the strongest constraint on the proton luminosity is given by gamma-ray observations via neutral pion decay $\pi^0 \rightarrow \gamma\gamma$ (de Jager et al. 1996; Aharonian et al. 2000; Amato et al. 2003). For $\Gamma \geqslant 10^6$, neutrino observations give additional information, and large values of $\Gamma = 10^7$ are exclusively observable by neutrinos, due to the high-energy spectrum. Di Palma et al. (2016) revise the predictions for pulsar wind nebulae (PWNe) given new TeV γ-ray observations (Aliu et al. 2008, 2013), predicting ∼13.09 neutrino events from the Crab Nebula per year in the energy range from 1 to 100 TeV. IceCube's 90% upper limit at the position of the Crab Nebula (see Table 2) constrains the number of neutrinos from the source to not more than 7.0 or 21.2 for an unbroken spectrum of E^{-2} and E^{-3}, respectively, from a total of 7 yr of data-taking. This is much lower than the predicted number of neutrino events during the same time range.

The second neutrino spectrum tested for the Crab Nebula is the one by Kappes et al. (2007; blue). The neutrino spectrum is connected to γ-rays assuming that both spectra originate from the same pion component. Thus, the resulting neutrino spectrum is fitted to an exponentially cutoff power-law $d\phi/dE_\nu \propto E^{-2.15} \exp\left(-\sqrt{E_\nu/1.72\ {\rm TeV}}\right)$. Due to the observed overfluctuation at the position of the Crab Nebula, the 90% upper limit regarding this model exceeds the benchmark model of 100% pion contribution by a factor of 1.18 and is thus not constraining the amount of hadronic acceleration. Nevertheless, IceCube's sensitivity (blue dashed line in Figure 11) is 15% below the model. Hence, with 7 yr of exposure, IceCube is now also sensitive to neutrino fluxes comparable to that of the Crab Nebula in gamma rays, i.e., bright but falling off at relatively low energies of a few TeV.

Another promising category of neutrino emitters are active galactic nuclei (AGNs), especially blazars of type BL Lac, as, for example, highlighted in Padovani & Resconi (2014). In Glüsenkamp (2015), an analysis of IceCube neutrino events

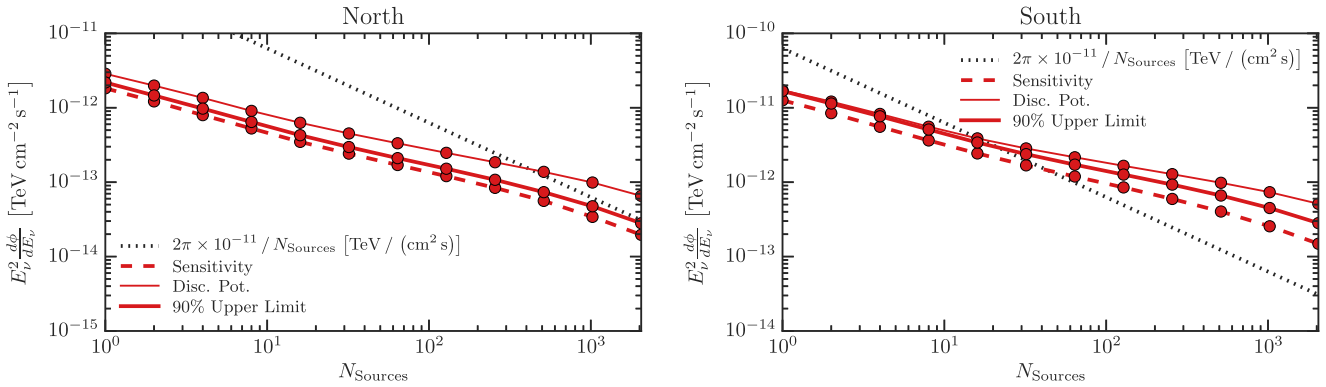

Figure 10. Discovery potential (5σ, solid thin line), sensitivity (dashed line), and 90% upper limit (solid thick line) for an unbroken E^{-2} spectrum in the population analysis for northern (left) and southern (right) sky, respectively. The flux is shown per source for increasing number of sources distributed uniformly on half of the sky. The black dashed line shows the IceCube-measured astrophysical neutrino flux per source if it was distributed homogeneously among $N_{\rm Sources}$ sources in this half of the sky.

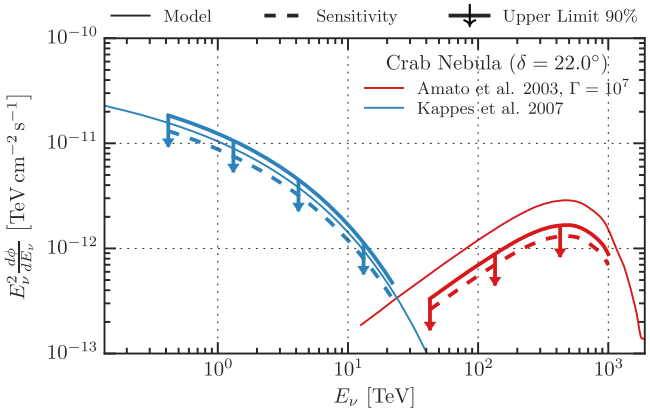

Figure 11. Differential $\nu_\mu + \bar{\nu}_\mu$ energy spectra vs. neutrino energy for the Crab Nebula. The figure shows the conversion of the observed gamma-ray flux of the Crab Nebula to neutrinos (Kappes et al. 2007) (blue) and a simulation of inelastic p–p scattering at the source (Amato et al. 2003) (red). Thick lines correspond to the 90% upper limit of this search; thin lines represent the model. The sensitivity of this analysis is shown as a dashed line. The 90% upper limit and sensitivity are shown for the energy interval, where 90% of the events originate that are most signal-like; see Figure 5.

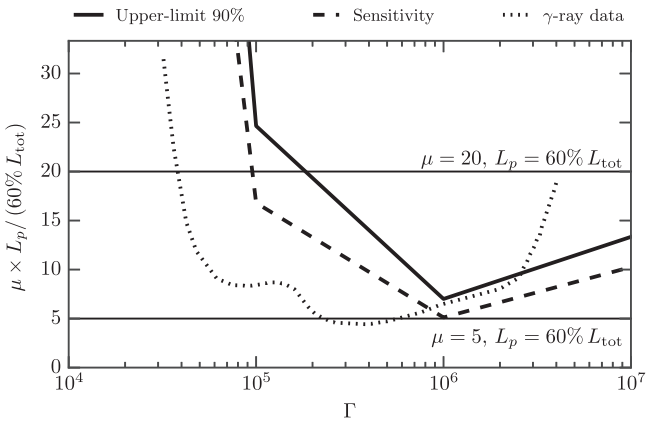

Figure 12. Sensitivity and 90% upper limit (dashed and solid lines, respectively) for the proton wind luminosity $L_{\rm p}$ and target density in Equation (7) of the Crab Nebula in Amato et al. (2003) for different Lorentz factors Γ. Values of $\mu = 20$ and $\mu = 5$ ($L_{\rm p} = 60\%\, L_{\rm tot}$) are indicated as horizontal lines that correspond to upper limits of the target density and a uniform mass distribution in the nebula, respectively. The dotted line indicates upper limits from gamma-ray observations compared to $\pi^0 \rightarrow \gamma\gamma$ decays (de Jager et al. 1996; Aharonian et al. 2000; Amato et al. 2003).

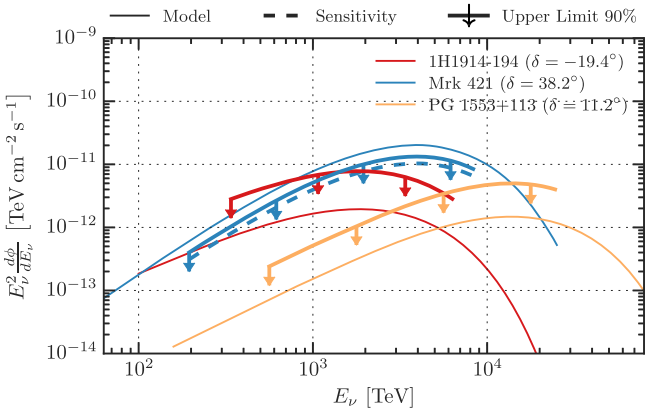

Figure 13. Same as Figure 11 for blazars of type BL Lac modeled in Petropoulou et al. (2015).

searched for correlations with blazars detected by *Fermi*-LAT to probe their possible connection to the observed diffuse astrophysical neutrino signal. It was found that such AGNs cannot be the dominant contribution to the diffuse neutrino flux over the entire probed energy range, but BL Lacs could possibly explain the high-energy part of the flux (Padovani et al. 2015). In Petropoulou et al. (2015), BL Lacs that were found to be in spatial and energetic agreement with IceCube high-energy starting events were modeled using lepto-hadronic fitting of multiwavelength data. Of the six modeled blazars, three are far from being constrained by IceCube, due to neutrino absorption in Earth (1ES 1011+496) or large atmospheric background deep in the southern sky (H2356-309, 1RXS J05435-5532). Figure 13 shows the expected neutrino energy spectra for the three remaining BL Lacs. The 90% upper limit for 1H 1914-194, also in the southern sky, is a factor of 3.9 above the prediction. For PG 1553 + 113, the contribution of proton–pion interactions in the model is small (total neutrino flux relative to TeV γ-ray flux $Y_\nu\gamma = 0.1$, Equation (13) in Petropoulou et al. 2015), resulting in a lower neutrino luminosity and a 90% upper limit of a factor of three above the prediction.

The third model source considered here is Mrk 421 (blue) and shows a different picture. Mrk 421 is one of the closest blazars with redshift $z \sim 0.03$ and with $\delta = 38.^\circ 2$, and it is located in the up-going region, where IceCube is most sensitive. Moreover, in Petropoulou et al. (2015), the

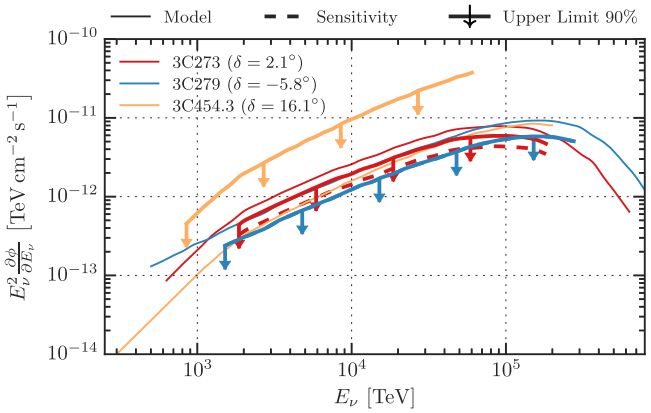

Figure 14. Same as Figure 11, but for blazars modeled in Reimer (2015).

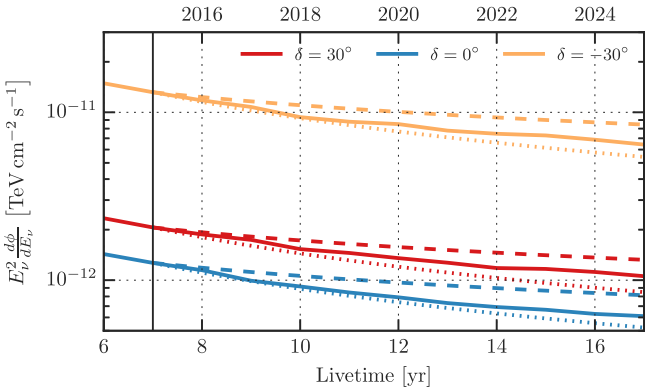

Figure 15. Time evolution in discovery potential (5σ) with increasing detector exposure. Different declinations are shown in different colors. The current status of this analysis corresponds to 7 yr or the year 2015 (indicated by vertical black line). Dashed lines indicate the sensitivity growth assuming a dependence with $1/\sqrt{T}$, dotted with $1/T$.

multiwavelength data observed can be explained with a very high hadronic component ($Y_\nu\gamma = 0.7$), thus realizing a high neutrino luminosity. For such a model, the 90% upper limit obtained by IceCube is 2/3 of the predicted neutrino flux. Hence, using the results at the position of Mrk 421, the hadronic acceleration cannot be bigger than $Y_\nu\gamma \leqslant 0.47$ assuming a steady emission over the 7 yr of analyzed data, and thus constrains proton luminosity of the source for steady emission or emission taking into account variability of the source (Petropoulou et al. 2015, 2016).

Other models for AGNs of type FSRQ or BL Lac were modeled in Reimer (2015). In Figure 14, 90% upper limits for 3C 273 (red), 3C 279 (blue), and 3C 454.3 (yellow) are shown. The models in this reference are very characteristic, due to their hard spectra extending beyond 10 PeV before cutting off. Hence, IceCube cannot constrain the prediction for FSRQ 3C 454.3 ($\delta = 16.^\circ1$) because most of the flux is absorbed in Earth and the 90% upper limit is a factor of five higher than the prediction. The two other FSRQs, on the other hand, are close to the horizon, where no absorption is present. Therefore, the 90% upper limit placed by IceCube is lower than the prediction, that is, 13% and 40% for 3C 273 and 3C 279, respectively. Similar to Mrk 421 in the previous paragraph, assuming that the emission is constant over the livetime of IceCube, this result constrains the amount of hadronic acceleration possible due to a nonobservation of neutrinos by IceCube with respect to the model prediction. The other AGNs modeled in Reimer (2015) are in the northern sky and due to absorption; the 90% upper limit by IceCube is at least a factor of 60 above the prediction.

Other models that were tested include galactic source-like supernova remnants (Mandelartz & Becker Tjus 2015) and unidentified TeV sources in the Galaxy (Fox et al. 2013) that are mainly in the southern sky, which coincides with most of the Galactic plane. There, IceCube has to cope with large atmospheric muon backgrounds and has reduced sensitivity with high energy thresholds; compare Figures 5 and 8. Consequently, the current 90% upper limits are at least a factor of five (G40.5–05; Mandelartz & Becker Tjus 2015) up to more than 100 (Vela X; Kappes et al. 2007) above the prediction. At these energies in the southern sky region, neutrino telescopes located in the northern hemisphere can place stronger constraints (Adrian-Martinez et al. 2015; Trovato 2016).

5. Conclusions

Analyzing the full sky for clustering of astrophysical neutrinos using 7 yr of through-going muon data from 2008 to 2015 and 5 yr of starting tracks (2010–2015), we did not find any significant steady point-like emission over the background expectation.

An unbiased scan of the full sky was performed, as well as dedicated searches using promising γ-ray candidates and searches for populations of weak sources. Results are consistent with background, and 90% upper limits on steady neutrino emission are calculated from the observations. In the northern sky ($\delta \geqslant 5°$), the best limits are set by IceCube and the sensitivity is below $E_\nu^2 d\phi/dE_\nu < 10^{-12}$ TeV cm^{-2} s^{-1} over a wide declination for the first time; compare Figure 8. Moreover, the declination-dependent flux limit is a factor of $\sim$100 ($\sim$10) below the integrated diffuse astrophysical neutrino flux in the northern (southern) sky. With increased statistics of three additional years compared to the previous analysis, the upper limits in the southern sky are of the same level as for Adrian-Martinez et al. (2014), however, testing a complementary energy region above PeV neutrino energies. Model-specific 90% upper limits were calculated for representative cases from the literature, and previously unconstrained neutrino emission scenarios for sources in the northern sky are now disfavored by IceCube. With the newly available data presented here, improved results for other tests are anticipated, for example, searches for extended sources or stacking and time-dependent analyses (Aartsen et al. 2014e, 2015e).

With increasing exposure, IceCube continues to improve the sensitivity to steady neutrino fluxes. Figure 15 shows the progression of the 5σ discovery potential with increasing time for three declinations. A continuous gain in performance is observed with time T that is faster than $1/\sqrt{T}$, a scenario assuming statistical limitation by background, and much closer to $1/T$, indicating limitation by signal statistics. This can increase even further with anticipated improvements in background rejection, angular reconstruction, or detector improvements (Aartsen et al. 2014b).

We acknowledge the support from the following agencies: U.S. National Science Foundation–Office of Polar Programs, U.S. National Science Foundation–Physics Division, University of Wisconsin Alumni Research Foundation, the Grid

Laboratory Of Wisconsin (GLOW) grid infrastructure at the University of Wisconsin–Madison, the Open Science Grid (OSG) grid infrastructure; U.S. Department of Energy, and National Energy Research Scientific Computing Center, the Louisiana Optical Network Initiative (LONI) grid computing resources; Natural Sciences and Engineering Research Council of Canada, WestGrid and Compute/Calcul Canada; Swedish Research Council, Swedish Polar Research Secretariat, Swedish National Infrastructure for Computing (SNIC), and Knut and Alice Wallenberg Foundation, Sweden; German Ministry for Education and Research (BMBF), Deutsche Forschungsgemeinschaft (DFG), Helmholtz Alliance for Astroparticle Physics (HAP), Research Department of Plasmas with Complex Interactions (Bochum), Germany; Fund for Scientific Research (FNRS-FWO), FWO Odysseus program, Flanders Institute to encourage scientific and technological research in industry (IWT), Belgian Federal Science Policy Office (Belspo); University of Oxford, United Kingdom; Marsden Fund, New Zealand; Australian Research Council; Japan Society for Promotion of Science (JSPS); the Swiss National Science Foundation (SNSF), Switzerland; National Research Foundation of Korea (NRF); Villum Fonden, Danish National Research Foundation (DNRF), Denmark.

References

Aartsen, M. G., Abbasi, R., Abdou, Y., et al. 2013a, Sci, 342, 1242856
Aartsen, M. G., Abbasi, R., Abdou, Y., et al. 2013b, NIMPA, A711, 73
Aartsen, M. G., Abbasi, R., Abdou, Y., et al. 2013c, ApJ, 779, 132
Aartsen, M. G., Abbasi, R., Abdou, Y., et al. 2014d, PhRv, D89, 102004
Aartsen, M. G., Abbasi, R., Ackermann, M., et al. 2014a, JINST, 9, 03009
Aartsen, M. G., Abraham, K., Ackermann, M., et al. 2015a, ApJ, 809, 98
Aartsen, M. G., Abraham, K., Ackermann, M., et al. 2015c, PhRvL, 115, 081102
Aartsen, M. G., Abraham, K., Ackermann, M., et al. 2015f, arXiv:1510.05223
Aartsen, M. G., Abraham, K., Ackermann, M., et al. 2016a, ApJ, 824, L28
Aartsen, M. G., Abraham, K., Ackermann, M., et al. 2016b, ApJ, 833, 3
Aartsen, M. G., Abraham, K., Ackermann, M., et al. 2016c, PhRv, D93, 022001
Aartsen, M. G., Ackermann, M., Adams, J., et al. 2014b, arXiv:1412.5106
Aartsen, M. G., Ackermann, M., Adams, J., et al. 2014c, PhRvL, 113, 101101
Aartsen, M. G., Ackermann, M., Adams, J., et al. 2014e, ApJ, 796, 109
Aartsen, M. G., Ackermann, M., Adams, J., et al. 2015b, PhRv, D91, 022001
Aartsen, M. G., Ackermann, M., Adams, J., et al. 2015d, PhRvL, 114, 171102
Aartsen, M. G., Ackermann, M., Adams, J., et al. 2015e, ApJ, 807, 46
Abbasi, R., Abdou, Y., Abu-Zayyad, T., et al. 2010, NIMPA, A618, 139
Abbasi, R., Abdou, Y., Abu-Zayyad, T., et al. 2011, ApJ, 732, 18
Abbasi, R., Abdou, Y., Abu-Zayyad, T., et al. 2012, APh, 35, 615
Abbasi, R., Abdou, Y., Ackermann, M., et al. 2013, NIMPA, A700, 188
Abbasi, R., Ackermann, M., Adams, J., et al. 2009, NIMPA, A601, 294
Abramowicz, H., Levin, E. M., Levy, A., & Maor, U. 1991, PhL, B269, 465
Abramowicz, H., & Levy, A. 1997, arXiv:hep-ph/9712415
Achterberg, A., Ackermann, M., Adams, J., et al. 2006, APh, 26, 155
Adrian-Martinez, S., Albert, A., André, M., et al. 2014, ApJ, 786, L5
Adrian-Martinez, S., Akhperjanian, A. G., Barrio, J. A., et al. 2015, arXiv:1511.02149
Aharonian, F. A., Akhperjanian, A. G., Barrio, J. A., et al. 2000, ApJ, 539, 317
Aliu, E., Anderhub, H., Antonelli, L. A., et al. 2008, Sci, 322, 1221
Aliu, E., Archambault, S., Arlen, T., et al. 2013, ApJ, 764, 38
Amato, E., Guetta, D., & Blasi, P. 2003, A&A, 402, 827
Anchordoqui, L. A., Barger, V., Cholis, I., et al. 2014, JHEAp, 1-2, 1
Anchordoqui, L. A., & Montaruli, T. 2010, ARNPS, 60, 129
Athar, H., Kim, C. S., & Lee, J. 2006, MPLA, A21, 1049
Atoyan, A. M., & Aharonian, F. A. 1996, MNRAS, 278, 525
Beatty, J. J., & Westerhoff, S. 2009, ARNPS, 59, 319
Braun, J., Dumm, J., De Palma, F., et al. 2008, APh, 29, 299
Bugaev, E. V., & Shlepin, Y. V. 2003a, NuPhS, 122, 341
Bugaev, E. V., & Shlepin, Y. V. 2003b, PhRv, D67, 034027
Chirkin, D., & Rhode, W. 2004, arXiv:hep-ph/0407075
de Jager, O. C., Harding, A. K., Michelson, P. F., et al. 1996, ApJ, 457, 253
Di Palma, I., Guetta, D., & Amato, E. 2016, arXiv:1605.01205
Fox, D. B., Kashiyama, K., & Mészarós, P. 2013, ApJ, 774, 74
Gaisser, T. K., Jero, K., Karle, A., & van Santen, J. 2014, PhRv, D90, 023009
Glashow, S. L. 1960, PhRv, 118, 316
Glüsenkamp, T. 2015, in 5th Roma Int. Conf. on Astro-Particle Physics (RICAP 14), ed. P. Piatelli et al., 05006
Gorski, K. M., Hivon, E., Banday, A. J., et al. 2005, ApJ, 622, 759
Halzen, F., & Hooper, D. 2002, RPPh, 65, 1025
Hinton, J. A., & Hofmann, W. 2009, ARA&A, 47, 523
Honda, M., Kajita, T., Kasahara, K., Midorikawa, S., & Sanuki, T. 2007, PhRv, D75, 043006
Jeong, Y. S., & Reno, M. H. 2010, PhRv, D82, 033010
Kappes, A., Hinton, J., Stegmann, C., & Aharonian, F. A. 2007, ApJ, 656, 870
Kotera, K., & Olinto, A. V. 2011, ARA&A, 49, 119
Learned, J. G., & Mannheim, K. 2000, ARNPS, 50, 679
Mandelartz, M., & Becker Tjus, J. 2015, APh, 65, 80
Murase, K., Guetta, D., & Ahlers, M. 2016, PhRvL, 116, 071101
Neunhöffer, T. 2006, APh, 25, 220
Olive, K. A., Agashe, K., Amsler, C., et al. 2014, ChPh, C38, 090001
Padovani, P., Petropoulou, M., Giommi, P., & Resconi, E. 2015, MNRAS, 452, 1877
Padovani, P., & Resconi, E. 2014, MNRAS, 443, 474
Petropoulou, M., Coenders, S., & Dimitrakoudis, S. 2016, APh, 80, 115
Petropoulou, M., Dimitrakoudis, S., Padovani, P., Mastichiadis, A., & Resconi, E. 2015, MNRAS, 448, 2412
Reimer, A. 2015, The 34th Int. Cosmic Ray Conf., ed. M. van den Berg et al., 1123
Schoenen, S., & Rädel, L. 2015, ATel, 7856
Schönert, S., Gaisser, T. K., Resconi, E., & Schulz, O. 2009, PhRv, D79, 043009
Senno, N., Murase, K., & Meszaros, P. 2016, PhRv, D93, 083003
Trovato, A. 2016, in 5th Roma Int. Conf. on Astro-Particle Physics (RICAP 14), ed. P. Piatelli et al., 05011